





Indoor Lidar Plenoptic Array Based on Time-of-Flight Reflection

Xuemei Wang , Collin Burt , *Member, IEEE*, Payman Zarkesh-Ha , *Senior Member, IEEE*, Alexander Neumann , and S. R. J. Brueck , *Fellow, IEEE*

Abstract—Improved energy efficiency and the associated cost savings is critical for environmental stewardship. In heating, ventilation, and cooling (HVAC) systems, occupancy sensors play an important role in system control for energy conservation. This paper introduces an integrated plenoptic device/people occupancy counting sensor for time-of-flight (ToF) measurements based on grating-coupled-waveguide, angularly resolved detection. Light from a 940 nm laser source is scattered from objects up to 5-m distant. The acceptance angle for scattered light is determined by the period of the detector grating and the waveguide properties. As a consequence of the narrow-band optical coupling, the plenoptic sensor demonstrates a good immunity to background light sources, such as sunlight and incandescent room illumination. The conical acceptance angles (azimuth and altitude) of this device are measured and confirm the device model. Importantly, the device is realized on a commercial silicon-based integrated-photonics foundry line, providing a pathway to volume manufacturing.

Index Terms—Integrated photonics, grating coupled waveguides, time-of-flight sensing.

I. INTRODUCTION

THERE is increasing interest in 3D optical measurements (azimuth, altitude and range) for applications ranging from automotive lidar [1], [2], to manufacturing processes [3], [4], occupancy detection [5], and healthcare [6]. System requirements including: range; resolution; field-of-view; ambient light rejection; multi-target array detection capability; power consumption; and eye safety vary across these applications. In general, time of flight distance sensors consist of a light source and a photodetector [7], [8], [9]. For indoor monitoring, with applications to HVAC control (occupancy monitoring) and healthcare applications, for example nursing home patient monitoring, privacy concerns often preclude imaging solutions [10], [12]. Spectroscopy is a related area of application for integrated lab-on-a-chip sensors [7], [13], [14], [15], [16], [17].

One way to accomplish occupancy detection while maintaining personal privacy is to use ToF sensors [18], [19]. In general, ToF sensors consist of a light source and a light detector [20],

Manuscript received 10 October 2022; accepted 15 October 2022. Date of publication 19 October 2022; date of current version 26 October 2022. This work was supported by the Advanced Research Projects Agency—Energy (ARPA-e) Sensor Program under Grant DE-AR0000942 through a subcontract from Rensselaer Polytechnic Institute. (*Corresponding author: S. R. J. Brueck.*)

The authors are with the Center for High Technology Materials, University of New Mexico, Albuquerque, NM 87131 USA (e-mail: xmei15wang@unm.edu; cburt2@unm.edu; payman@ece.unm.edu; aneumann@chtm.unm.edu; brueck@chtm.unm.edu).

Digital Object Identifier 10.1109/JPHOT.2022.3215482

[21]. The light source can be a laser emitting a pulsed or a continuous-wave signal. When this signal illuminates an object, some of that light is scattered back towards the detector. The ToF sensor measures the time for the transmitted light signal to return to the detector, providing a distance measurement. Adding an array of detectors with specific angular acceptance provides a 3D capability, giving the distance to objects and their orientation relative to the sensor. This is not a stereoscopic measurement and is independent of the size of the detection array. Building occupancy monitoring is an important application that could lead to substantial reductions in HVAC energy usage and play an important role in environmental stewardship. Clearly cost considerations require monitoring of wide areas with ToF sensor arrays. Integrated photonic optical sensors, compatible with high volume silicon integrated circuit manufacturing, are essential for reaching system cost goals and widespread adoption [22]. A significant issue for ToF sensors is interference between the TOF signal and room illumination (including sunlight). Most commercial ToF systems used broadband single photon avalanche detectors (SPADs). Spectral filters help in rejecting room illumination, but are still relatively broadband posing a significant issue [23], [24].

II. GRATING COUPLING TO PLANAR WAVEGUIDE

This paper presents initial experimental results for a novel plenoptic (angle of incidence and wavelength) sensor designed specifically for maintaining personal privacy while performing occupancy detection via ToF measurements. Importantly, the sensor was fabricated in an integrated-photonics foundry process. The goal is to fabricate an array of sensors with different gratings looking in many different directions and covering a large azimuth/altitude footprint, with standard microelectronic manufacturing enabling low-cost mass production. Unlike the photodetectors used in cameras or other lidar systems that accept light from a cone of incident directions, a grating coupler is used to filter the reflected light such that each detector receives light from a specific set of azimuthal (ϕ) and altitude (θ) angles and in a narrow wavelength range providing enhanced rejection of background illumination. Whereas traditional ToF systems look in a small number of directions and determine the distance to an object, combining the angle discrimination of an array of plenoptic devices with a ToF measurement allows the position of multiple objects to be determined, in effect a coarse 3D mapping. For a fixed wavelength (λ) and structure of the waveguide ($n_{mode}^{TE, TM}$), the angles of altitude and azimuthal incidence

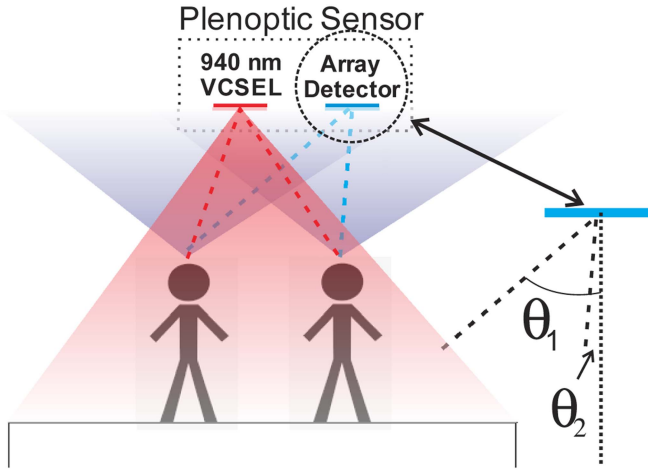


Fig. 1. Concept of plenoptic sensor array. A source on the ceiling illuminates a cone, time-of-flight of reflected light is detected at multiple angles to provide a coarse 3D mapping. For simplicity of depiction, the azimuth $\phi = 0$ in the figure.

(θ, ϕ) that are coupled into the waveguide are determined by the period of the grating (d). Fig. 1 shows a schematic of the system design. A 940 nm VCSEL emits light that is reflected from an object, such as the head of a person, back towards an array of plenoptic sensors with different grating periods and orientations. Light is coupled into one or more sensors, and is rejected by others, due to the varying phase matching constraints resulting from the different gratings. The coupled signal is detected by a photodiode integrated with the waveguide and is then amplified by a transimpedance amplifier (TIA). The ToF distance determination can be either direct (using ns pulses) or indirect (phase shift of an amplitude-modulated CW signal). We provide an initial demonstration using indirect ToF. For occupancy counting, the sensor array and laser will be mounted on the ceiling; therefore, distance measurements and conical diffraction are also considered here. The signal-to-noise ratio of the detector allows for accurate free-space measurements to be taken over a distance of a few meters, even when considering background noise sources such as sunlight or room illumination. The range will be set by eye-safety considerations, a range of ~ 5 m is demonstrated with a commercial laser source.

The coupling angles are determined by phase matching between the incident wavevector $k_x(\theta, \phi) = 2\pi/\lambda \sin \theta \cos \phi$; $k_y(\theta, \phi) = 2\pi/\lambda \sin \theta \sin \phi$ scattered by the grating, $\Delta k_x = m2\pi/d$, where λ is the source wavelength, d is the grating period, m is an integer (+1 for the experiments reported here), and the modal wavevector is $2\pi/\lambda n_{mode}^{TE, TM}(\lambda)$.

$$k_x(\theta, \phi) = \frac{2\pi}{\lambda} \left(\sin \theta \cos \phi \pm m \frac{\lambda}{d} \right);$$

$$k_y(\theta, \phi) = \frac{2\pi}{\lambda} \sin \theta \sin \phi;$$

$$k_x^2(\theta, \phi) + k_y^2(\theta, \phi) = \left[\frac{2\pi}{\lambda} n_{mode}^{TE, TM}(\lambda) \right]^2 \quad (1)$$

In the limit of $\phi = 0$, these equations simplify to the more familiar grating equation, $\sin \theta \pm m \lambda/d = \pm n_{mode}^{TE, TM}$, where

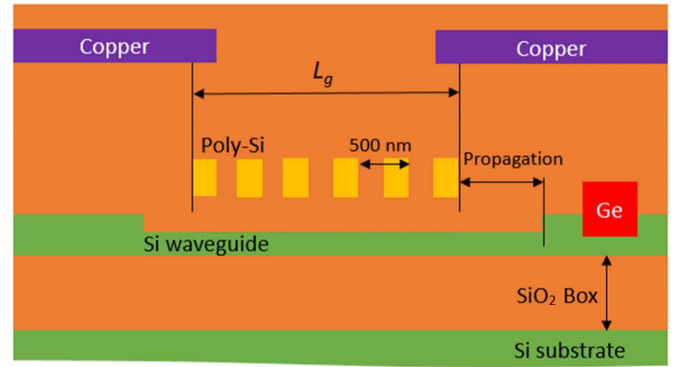


Fig. 2. The schematic of the plenoptic device based on a SOI waveguide clad with SiO₂, a poly-Si grating structure and a Ge photodetector.

the plus (minus) signs are for forward (backward) coupling. First, results are presented for $\phi = 0$ to establish the coupling properties; conical coupling ($\phi \neq 0$) is then discussed.

III. DESIGN AND SIMULATION

The collection area and the photodetector of the sensor are integrated on chip and fabricated in a commercial silicon-on-insulator (SOI) integrated-photonics foundry process. A thinned silicon waveguide layer was chosen to reduce silicon absorption losses at the 940 nm design wavelength. The schematic structure of a typical plenoptic device is shown in Fig. 2. Other variations including an un-thinned silicon waveguide layer and a silicon nitride waveguide core layer have been investigated and will be reported elsewhere. The refractive index of Si at 940 nm is $3.6 + i1.37 \times 10^{-3}$ [25]. The waveguide and gratings are comprised of Si and poly-Si, respectively. The modal indices in the absence of the poly-Si grating are TE: $2.26 + i1 \times 10^{-3}$ and TM: $1.54 + i4.2 \times 10^{-5}$; the TE mode is more strongly confined in the silicon layer and has a correspondingly higher loss. The 1/e propagation length for the TE (TM) mode is $\sim 150 \mu\text{m}$ (3.6 mm) while the distance between the collection and detection is only ~ 15 - to 30 - μm , so propagation losses are negligible for the TM mode and relatively minor for the TE mode. For the present demonstration, the period of the grating is 500 nm, with a line:space ratio of 0.32. A heteroepitaxial Ge absorption region, partially embedded in the silicon layer is used to detect the 940 nm waveguide mode power. Shielding to prevent direct illumination of the detector is incorporated into the back-end-of-the-line metallization layers.

The finite-difference time-domain (FDTD) simulation results for the collection of incident illumination are presented in Fig. 3. Because the TM mode propagates in the backward direction, the coupling angle is negative. Four factors influence $\Delta\theta$, the angular width of the coupling: the coupling length L_c , the 1/e length over which light is coupled out of the waveguide by the grating; the coupling angle, θ ; the physical length of the collection area grating parallel to the grating lines, L_g ; and the extent of the illumination spot. In the plenoptic measurement outlined in Fig. 1, the illumination is always much wider than the device. For simulation purposes, the laser source is treated as an ideal plane wave. For the case $L_c \gtrsim L_g$, the angular lineshape is

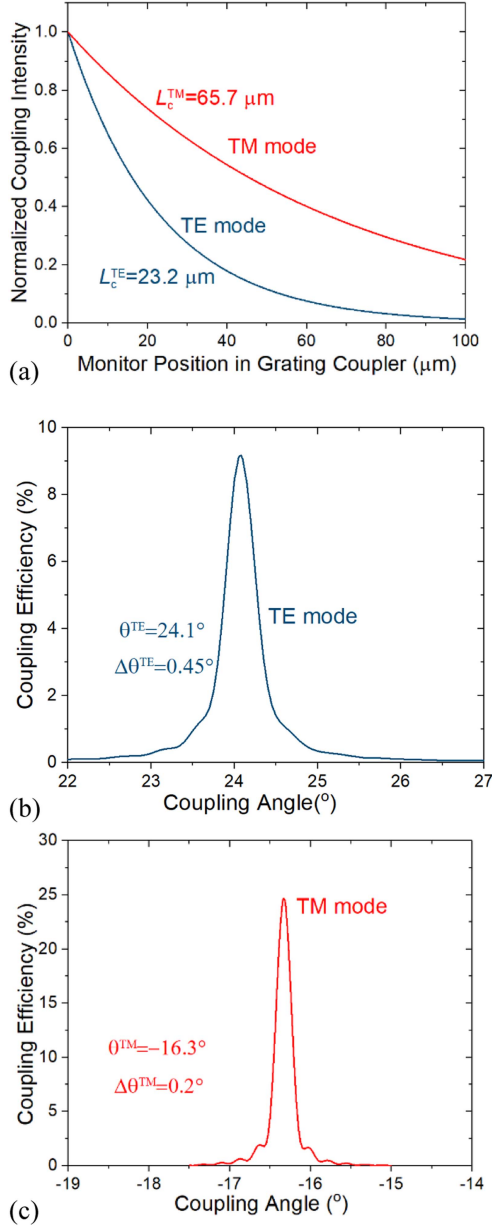


Fig. 3. The simulation result of (a) coupling length and angular intensity for (b) TE and (c) TM mode coupling. (a) shows the decay of the signal power in the waveguide as a function of propagation length from the start of the grating. The collection area length was $250 \mu\text{m}$, sufficiently long that the angular width is inversely proportional to the coupling length. The $250 \mu\text{m}$ TE mode collection length is more than 10x the simulated coupling length, so the resolution is dominated by L_c . The angular resolution of the TM mode is narrower than that for the TE mode as a result of the longer L_c ; there is some contribution to the angular resolution from the finite grating dimension (L_g) as well as from the coupling length.

a sinc function and the angular width is dominantly inverse to L_g . When the $L_g \geq 4L_c$, the acceptance angle is set by the coupling length and the altitude angle and the lineshape is Lorentzian [15], [26]:

$$\Delta\theta = \frac{\lambda}{2\pi L_c \cos \theta} \quad (2)$$

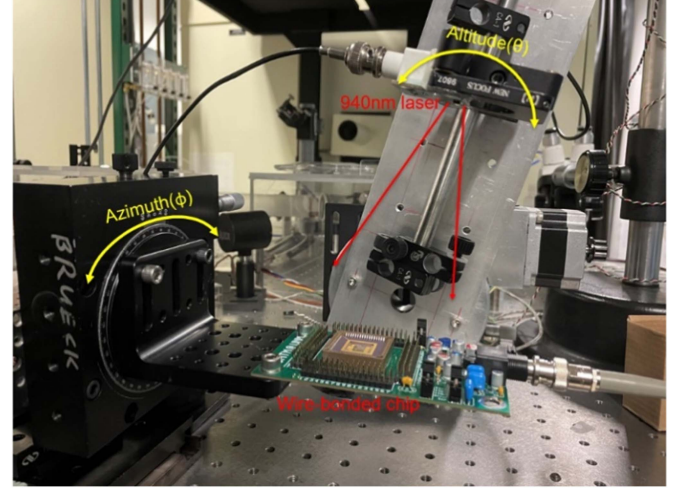


Fig. 4. The experimental setup for the angular scan.

Here $\Delta\theta$ is the acceptance angle, θ is the coupling angle and L_c is the coupling length. The wavelength range for coupling at a fixed angle is closely related, and will be important for broadband background rejection as discussed below:

$$\begin{aligned} \Delta\lambda &= \frac{\lambda d}{2\pi L_c \left[1 - d \left(\frac{\partial n_{mode}}{\partial \lambda} \right) \right]} \\ &= \frac{d\Delta\theta \cos \theta}{\left[1 - d \left(\frac{\partial n_{mode}}{\partial \lambda} \right) \right]} \end{aligned} \quad (3)$$

In Fig. 3(a), the numerical simulation of L_c was performed by launching a mode under the grating and monitoring the decay of the modal intensity as power is radiated into free space. This is equivalent to the length for which additional energy is coupled into the waveguide mode under uniform irradiation. Any energy coupled in for longer grating dimensions is reradiated before it reaches the propagation region. The TE coupling is in the forward direction, while the lower modal index TM mode is backward coupled. The results for the angular width are consistent with the L_c calculations of (2). For an extended source, such as reflection from a person, the total intensity coupled into the waveguide mode is proportional to the product of the peak efficiency (11% - TE; 23% - TM) and the angular acceptance $\Delta\theta$. This product is 0.066 (TE) and 0.05 (TM), roughly comparable for the two polarizations.

IV. MEASUREMENT RESULTS AND ANALYSIS

A. 4.1 Coupling and Acceptance Angles

Fig. 4 shows the measurement arrangement. An Osram pulsed VCSEL 940 nm laser array (PLPVQ940A) was used as the source for the angular scan. The emission area of the device is $\sim 0.25 \text{ mm}^2$. The laser was positioned 12 cm above the device along the altitude axis. The azimuth angle is 0° for the coupling angle measurements. The illumination field of the laser is 65° along the horizontal axis and 78° along the vertical axis. The arm of the measurement instrument is rotated to find the coupling

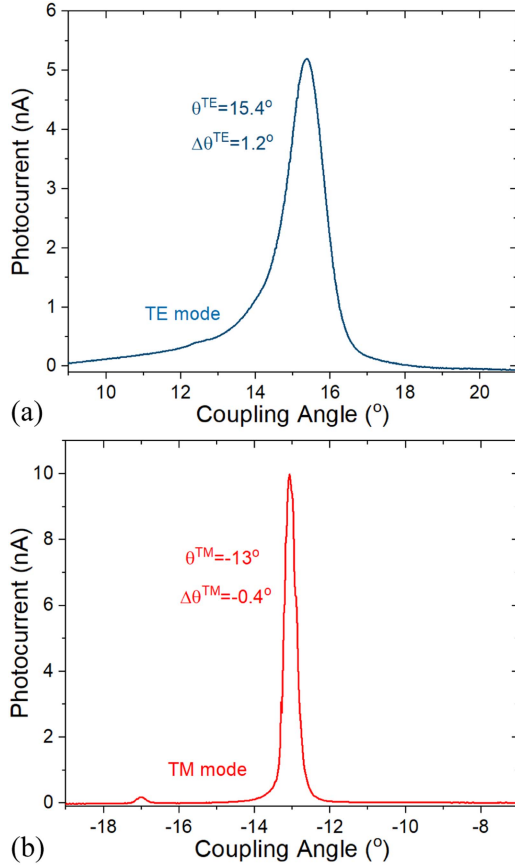


Fig. 5. Measurement result for (a) TE polarization and (b) TM polarization. The height of the gratings was $100\ \mu\text{m}$. The detectors were unbiased to eliminate noise due to dark current.

angle. The azimuth angle is then swept in 5° increments to monitor the conical diffraction variations.

Fig. 5 shows the $\phi = 0$ measurement of the (a) TE and (b) TM mode coupling angles with a 500-nm period poly-Si grating and a thinned SOI waveguide with the detector at 0 V bias. The grating height (along the grating lines) was $100\ \mu\text{m}$ and the power density incident on the chip before coupling was $26\ \mu\text{W}/\text{mm}^2$.

To fit these experimental results, the effective refractive index n_{eff} is adjusted from 1.62 to 1.65, this could be due to manufacturing variations in the thickness of the SOI waveguide or the grating period. The finite size of the laser array contributes about 0.2° to the acceptance angles. The results are in reasonable agreement with the simulation.

B. 4.2 Conical Coupling Angles

As devices will be assembled on the ceiling, the illumination will be incident on the grating in a conical geometry, where the in-plane component of the incident beam direction, depending on the position of the scatterer, is at an arbitrary angle to the grating k -vector. It is very important to understand the angular response for an arbitrary combination of (ϕ, θ) . Fig. 6 presents the angular response and photocurrent for TM-mode coupling in a conical geometry. The power density is $26\text{xcos}(\phi)\ \mu\text{W}/\text{mm}^2$. $\phi = 0$ corresponds to light incident along the grating k -vector.

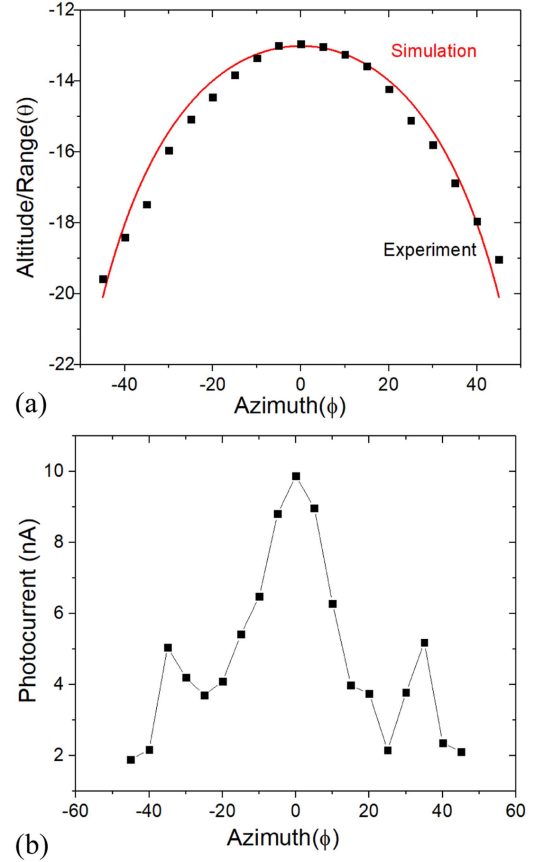


Fig. 6. (a) TM angular response for conical geometry and (b) photocurrent variation with azimuthal angle.

As a result of mechanical issues, the angular response and photocurrent are not perfectly symmetric. The phase-matching calculation is in good agreement with the experimental results. When $\phi = 0$, the lowest coupling angle -13° and the highest photocurrent are obtained. As the azimuth is increased, the coupling angle increases. The coupling angle varies from -13° to -19° with the azimuth angle varying from 0° to 45° . The results are in good agreement with the angles calculated from (1). The photocurrent decreases faster than $1/\text{cos}(\phi)$ since the mode propagates at an angle to the detector which is parallel to the grating lines and more and more of the collection area is lost as ϕ increases.

C. 4.3 Immunity to Background Illumination

Many time-of-flight systems are plagued by broadband background illumination, for example from sunlight or room illumination, that interferes with the measurements [27]. In contrast to direct measurement approaches, the waveguide coupling approach is sensitive only to a narrow wavelength band [$\Delta\lambda \sim d\Delta\theta^{TM}\text{cos}\theta^{TM} \sim 1.7\ \text{nm}$] rejecting most broadband background illumination.

Sunlight and incandescent room lighting have high irradiance around the 940 nm design wavelength, so interference from these sources must be considered [28], [29]. Most white LEDs are composed of blue LEDs along with a yellow phosphor. The

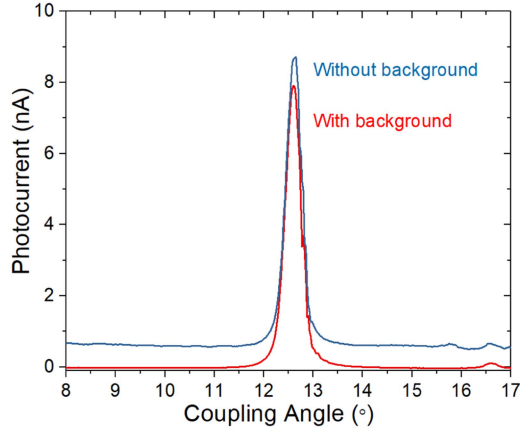


Fig. 7. Signal variation without and with incandescent light irradiation.

peaks of the spectrum are at 450 nm and 550 nm [30], and the interference due to LED lighting is generally negligible. Here, we present result for co-illumination with a 940 nm laser and an incandescent lamp source (500 lumens). The incandescent light color temperature is 2700 K and it is positioned 21 cm away from the chip. Since this is an extended source, the incident angle is over a range of $-13^\circ \pm 1.5^\circ$. The power density of the incandescent light on the chip is $13 \mu\text{W}/\text{mm}^2$, while the TM power density of the laser is $20.8 \mu\text{W}/\text{mm}^2$. Fig. 7 shows the TM measurement results with and without the incandescent light irradiance. Compared to the data without the background, the noise baseline increases to ~ 0.9 nA as a result of the broadband continuum emission of the incandescent lamp within the bandwidth of the grating coupler. Without the grating filtration, the signal from the broadband incandescent lamp would saturate the detector and totally swamp the received signal. The signal amplitude is unaffected and is simply additive to the background. The acceptance angle remains at 0.4° for both data sets. The background noise from sunshine and/or incandescent room illumination does not influence the accuracy of the plenoptic angle measurement.

D. 4.4 Demonstration of Indirect Time-of-Flight Measurements

This plenoptic detector can be used in either direct (pulse delay metric) or indirect (phase shift metric) ToF sensors, in this work we chose an indirect approach to demonstrate a practical use of plenoptic device in a ToF application as shown in Fig. 8. A commercial lock-in amplifier (Moku:Lab from Liquid Instruments [30]) was used to measure the phase/amplitude of the reflected beam from a target object compared to the reference source, which drives a 940 nm laser. A detailed systems analysis is underway to optimize the array performance.

The test setup is shown in Fig. 9, where a custom printed circuit board (PCB) was designed with a socket to hold the test chip with foundry-fabricated plenoptic devices. The PCB also contains an ultra-low noise ($250 \text{ fA}/\sqrt{\text{Hz}}$) and high gain ($10 \text{ M}\Omega$) transimpedance amplifier (TIA) The detector was operated a zero bias to eliminate dark current noise. While the

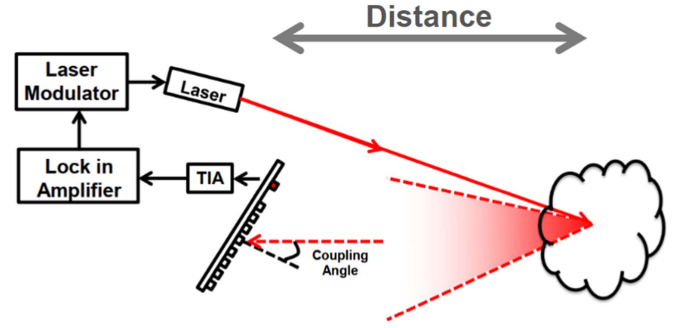


Fig. 8. Test setup using indirect ToF measurement using the developed plenoptic sensor.

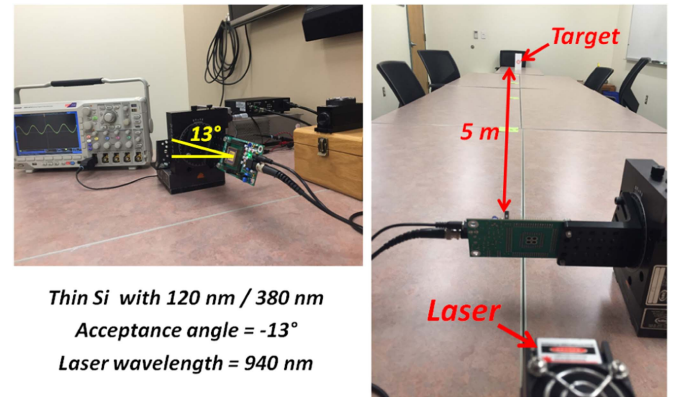


Fig. 9. Test setup for the demonstration of the ToF using fabricated thin Si waveguide. The reflected signal at 5 m range was successfully measured.

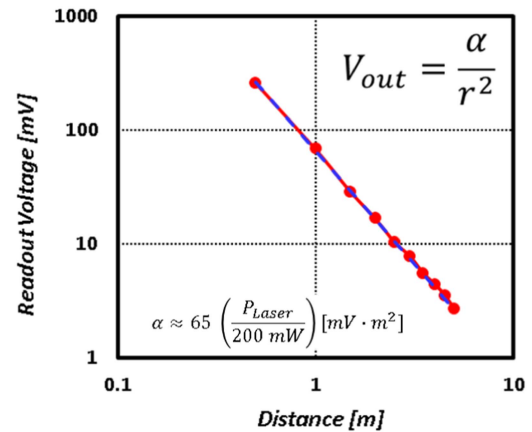


Fig. 10. The measured signal versus target distance up to 5 m range.

target was placed at various distances, the phase of the reflected signal was measured using a lock-in amplifier. The PCB holding the chip is mounted on a rotation stage, so that its angle can be adjusted to accept the reflected light at the coupling angle set by the plenoptic device under test as shown in Fig. 9.

The reflected signal at a 5 m range was successfully measured. Fig. 10 illustrates the measured signal, when the target is placed at various distances from the source/detector. The signal

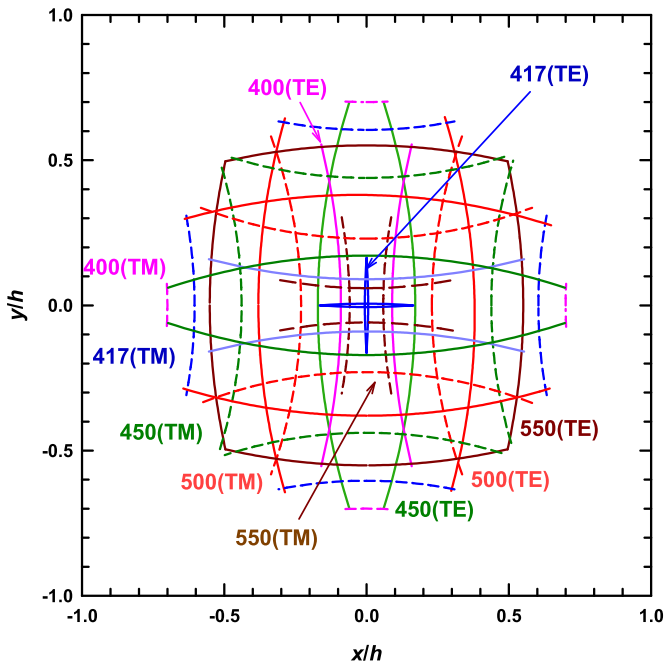


Fig. 11. Spatial coverage with a ten-element array with five periods (550-, 500-, 450-, 417- and 400-nm) and two perpendicular orientations. Five pixels with grating lines oriented in the x -direction and five oriented in the y -direction. The axes are normalized to the height of the sensor above the detection spherical section (set by the time-of-flight). The overall coverage approximates a circle with a radius of $h \sin \theta_{ill} = 0.707h$ where $\theta_{ill} = 45^\circ$ is the illumination half-angle. TE mode coupling is shown with solid lines, TM mode with dashed lines. The 417-nm period grating was chosen to be close to coupling at normal incidence for the TE mode, hence the star-shaped response at normal incidence to the sensor.

versus distance clearly follows the expected $1/R^2$ relationship. The device under the test had the same structure as the device reported in Figs. 5–7 with a thinned Si waveguide, with a $100 \mu\text{m}$ collection height, and a 500 nm period poly-Si coupling grating with a coupling angle of about -13° . The lock-in carrier frequency was 10.61 KHz and the average laser power was 200 mW. This frequency was chosen to accommodate the TIA bandwidth, and is too low for room occupancy distance measurements. The maximum range depends on several parameters including laser power, detector noise, TIA noise, as well as system bandwidth. Our measurement was limited by the background noise of the TIA. Avalanche detection, which boosts both the signal and the detector noise making the TIA noise less significant, will lead to a further extension in the range.

The measured data from this experiment provides a baseline that will be used to scale the design for commercially viable ToF sensor application, where the laser power will be reduced to an eye-safe range. The areas of improvement include collection area optimization, as well as APD optimization, and TIA integration.

V. DISCUSSION AND CONCLUSION

Grating-coupled plenoptic detectors provide angle of incidence information. These devices are readily integrated in silicon photonics and have myriad applications in automotive

control, environmental efficiency and energy saving, manufacturing, and healthcare. The integrated devices demonstrated here were fabricated in a commercial silicon-on-insulator integrated photonics 90 nm process. For a fixed 940 nm wavelength source, we have demonstrated angular sensitivities of 0.4° (1.2°) for TM (TE) light incident on a SOI-based waveguide with a poly-Si grating. The impact of conical illumination has been analyzed and demonstrated. Importantly, the waveguide configuration provides a narrow-band filtering function that makes these devices insensitive to broadband background illumination such as sunlight. An indirect TOF measurement with a range of up to 5 m has been demonstrated.

The next step is to fabricate an array with different period grating and different orientations. An initial system concept is shown in Fig. 11 which shows the spatial coverage with a 10-element array with five different period gratings oriented along orthogonal x - and y -directions. Detectors, parallel to the grating lines, are assumed on both sides of the collection area. TE-mode coupling is represented with solid lines, TM-mode coupling with dashed lines. The 417 nm period grating was chosen to provide approximately normal incidence coupling to the TE mode, resulting in the star-shaped response near $(0, 0)$. The overall response approximates the illumination circle with a radius of $0.707h$ where h is the height above the observation plane assuming a 45° $1/2$ -angle illumination cone. Additional gratings with intermediate periods will provide additional spatial resolution, if necessary. Coincidence detection, and continuity monitoring with multiple sensors at the same distance from the source will provide additional signal processing opportunity for confirming position and movement as people circulate in the room. The scale of the figure is normalized to the height from the sensor. For example, for a sensor mounted in an office space, assuming a 3 m ceiling height, the illuminated region on the floor corresponds to ~ 2 m. For a person standing under the sensor, the distance to the ceiling is ~ 1 m, and the circle roughly corresponds to a 0.7 m diameter, while the extended reflection occupies ~ 0.3 m, so this limited number of ToF sensors provides more than adequate resolution. For a larger conference venue, with for example a 7-m high ceiling, the diameter for a standing person is ~ 3.5 m and additional resolution (intermediate grating periods) will be required.

The next steps are to integrate the detection and analysis electronics, to fabricate arrays of devices with different grating periods and orientations to provide a low-resolution 3D mapping capability and to demonstrate indoor lidar with a co-packaged 940 nm source. This will provide a low-cost manufacturable solution that will enable many indoor lidar applications.

ACKNOWLEDGMENT

Professor Robert F. Karliceck (RPI) has led this effort in indoor lidar for application to buildings (HVAC) and healthcare. We gratefully acknowledge his leadership. We have benefited from many discussions with Prof. Mona Hella and Mr. John Rollinson (RPI). Global Foundries has provided multiple IC-foundry runs for these integrated plenoptic devices.

REFERENCES

- [1] R. Roriz, J. Cabral, and T. Gomes, "Automotive LiDAR technology: A survey," *IEEE Trans. Intell. Transp. Syst.*, vol. 23, no. 7, pp. 6282–6297, Jul. 2022, doi: [10.1109/TITS.2021.3086804](https://doi.org/10.1109/TITS.2021.3086804).
- [2] T. Liu, Q. Sun, Z. Fan, and Y. Jia, "TOF lidar development in autonomous vehicles," in *Proc. IEEE 3rd Optoelectron. Glob. Conf.*, 2018, pp. 185–190, doi: [10.1109/OGC.2018.8529992](https://doi.org/10.1109/OGC.2018.8529992).
- [3] J. Meng et al., "A safe and efficient LIDAR-based navigation system for 4WS4WD mobile manipulators in manufacturing plants," *Meas. Sci. Technol.*, vol. 32, 2021, Art. no. 045203, doi: [10.1088/1361-6501/abce71](https://doi.org/10.1088/1361-6501/abce71).
- [4] L. Zhang, J. Chen, C. Ma, W. Li, Z. Qi, and N. Xue, "Research progress on on-chip Fourier transform spectrometer," *Laser Photon. Rev.*, vol. 15, 2021, Art. no. 2100016, doi: [10.1002/lpor.202100016](https://doi.org/10.1002/lpor.202100016).
- [5] A. K. Chandran, A. Subramaniam, W. C. Wong, J. Yang, and K. A. Chaturvedi, "A PTZ camera-based people-occupancy estimation system (PCBPOES)," in *Proc. 15th IAPR Intl. Conf. Mach. Vis. Appl.*, 2017, pp. 145–148, doi: [10.23919/MVA.2017.7986822](https://doi.org/10.23919/MVA.2017.7986822).
- [6] M. Bouazizi, C. Ye, and T. Ohtsuki, "Activity detection using 2D LIDAR for healthcare and monitoring," in *Proc. IEEE Glob. Commun. Conf.*, 2021, pp. 1–6, doi: [10.1109/GLOBECOM46510.2021.9685470](https://doi.org/10.1109/GLOBECOM46510.2021.9685470).
- [7] M. S. Sruthi, "IoT based real time people counting system for smart buildings," *Int. J. Emerg. Technol. Innov. Eng.*, vol. 5, pp. 83–86, 2019. [Online]. Available: <https://ssrn.com/abstract=3340446>
- [8] M. Lindner, I. Schiller, A. Kolb, and R. Koch, "Time-of-flight sensor calibration for accurate range sensing," *Comp. Vis. Image Understanding*, vol. 114, no. 12, pp. 1318–1328, 2010, doi: [10.1016/j.cviu.2009.11.002](https://doi.org/10.1016/j.cviu.2009.11.002).
- [9] P. Preethi, C. Zhang, and E. Charbon, "Modeling and analysis of a direct time-of-flight sensor architecture for LiDAR applications," *Sensors*, vol. 19, no. 24, 2019, Art. no. 5464, doi: [10.3390/s19245464](https://doi.org/10.3390/s19245464).
- [10] D. N. Serpanos and A. Papalambrou, "Security and privacy in distributed smart cameras," *Proc. IEEE*, vol. 96, no. 10, pp. 1678–1687, Oct. 2008, doi: [10.1109/JPROC.2008.928763](https://doi.org/10.1109/JPROC.2008.928763).
- [11] D. Delibaltov, W. Wu, R. P. Loce, and E. A. Bernal, "Parking lot occupancy determination from lamp-post camera images," in *Proc. 16th Int. IEEE Conf. Intell. Transp. Syst.*, 2013, pp. 2387–2392, doi: [10.1109/ITSC.2013.6728584](https://doi.org/10.1109/ITSC.2013.6728584).
- [12] J.-H. Choi, J.-E. Kim, and K.-T. Kim, "People counting using IR-UWB radar sensor in a wide area," *IEEE Internet Things J.*, vol. 8, no. 7, pp. 5806–5821, Apr. 2021, doi: [10.1109/JIOT.2020.3032710](https://doi.org/10.1109/JIOT.2020.3032710).
- [13] X. Wang, V. Sasidharen, A. Neumann, P. Zarkesh-Ha, and S. R. J. Brueck, "Visible (400- to 700-nm) chirped-grating-coupled waveguide spectrometer," *Opt. Exp.*, vol. 30, no. 14, pp. 25050–25060, 2022, doi: [10.1364/OE.462781](https://doi.org/10.1364/OE.462781).
- [14] Z. Yang, T. Albrow-Owen, W. Cai, and T. Hasan, "Miniaturization of optical spectrometers," *Science*, vol. 371, 2021, Art. no. eab0722, doi: [10.1126/science.abe0722](https://doi.org/10.1126/science.abe0722).
- [15] S. Nezhadbadeh, A. Neumann, P. Zarkesh-Ha, and S. R. J. Brueck, "Chirped-grating spectrometer-on-a-chip," *Opt. Exp.*, vol. 28, no. 17, pp. 24501–24510, 2020, doi: [10.1364/OE.398072](https://doi.org/10.1364/OE.398072).
- [16] C. Rogers et al., "A universal 3D imaging sensor on a silicon photonics platform," *Nature*, vol. 590, pp. 256–261, 2021, doi: [10.1038/s41586-021-03259-y](https://doi.org/10.1038/s41586-021-03259-y).
- [17] Y. Kwak, S. M. Park, Z. Ku, A. Urbas, and Y. L. Kim, "A pearl spectrometer," *Nano Lett.*, vol. 21, no. 2, pp. 921–930, 2021, doi: [10.1021/acs.nanolett.0c03618](https://doi.org/10.1021/acs.nanolett.0c03618).
- [18] M. Lindner, I. Schiller, A. Kolb, and R. Koch, "Time-of-flight sensor calibration for accurate range sensing," *Comp. Vis. Image Understanding*, vol. 114, no. 12, pp. 1318–1328, 2010, doi: [10.1016/j.cviu.2009.11.002](https://doi.org/10.1016/j.cviu.2009.11.002).
- [19] C. Hong, S.-H. Kim, J.-H. Kim, and S. M. Park, "A linear-mode LiDAR sensor using a multi-channel CMOS transimpedance amplifier array," *IEEE Sensors J.*, vol. 18, no. 17, pp. 7032–7040, Sep. 2018, doi: [10.1109/JSEN.2018.2852794](https://doi.org/10.1109/JSEN.2018.2852794).
- [20] H. Seo et al., "Direct TOF scanning LiDAR sensor with two-step multivalent histogramming TDC and embedded interference filter," *IEEE J. Solid-State Circuits*, vol. 56, no. 4, pp. 1022–1035, Apr. 2021, doi: [10.1109/JSSC.2020.3048074](https://doi.org/10.1109/JSSC.2020.3048074).
- [21] P. Padmanabhan, C. Zhang, and E. Charbon, "Modeling and analysis of a direct time-of-flight sensor architecture for LiDAR applications," *Sensors*, vol. 19, no. 24, 2019, Art. no. 5464, doi: [10.3390/s19245464](https://doi.org/10.3390/s19245464).
- [22] H. Aasen, E. Honkavaara, A. Lucieer, and P. J. Zarco-Tejada, "Quantitative remote sensing at ultra-high resolution with UAV spectroscopy: A review of sensor technology, measurement procedures, and data correction workflows," *Remote Sens.*, vol. 10, 2021, Art. no. 1091, doi: [10.3390/rs10071091](https://doi.org/10.3390/rs10071091).
- [23] A. Süß, V. Rochus, M. Rosmeulen, and X. Rottenberg, "Benchmarking time-of-flight based depth measurement techniques," in *Proc. SPIE*, vol. 9751, 2016, Art. no. 975118, doi: [10.1117/12.2212478](https://doi.org/10.1117/12.2212478).
- [24] H. Seo et al., "A CMOS LiDAR sensor with pre-post histogramming for sunlight immunity over 105 klx and SPAD-based infinite interference cancelling," in *Proc. Symp. VLSI Circuits*, 2021, pp. 1–2.
- [25] C. Schinke et al., "Uncertainty analysis for the coefficient of band-to-band absorption of crystalline silicon," *AIP Adv.*, vol. 5, no. 6, 2015, Art. no. 067168, doi: [10.1063/1.4923379](https://doi.org/10.1063/1.4923379).
- [26] J. C. Brazas and L. Li, "Analysis of input-grating couplers having finite lengths," *Appl. Opt.*, vol. 34, no. 19, pp. 3786–3392, 1995.
- [27] L. Carrara and A. Fiergolski, "An optical interference suppression scheme for TCSPC flash LiDAR imagers," *Appl. Sci.*, vol. 9, no. 11, 2019, Art. no. 2206, doi: [10.3390/app9112206](https://doi.org/10.3390/app9112206).
- [28] I. Ermolli et al., "Recent variability of the solar spectral irradiance and its impact on climate modelling," *Atmosph. Chem. Phys.*, vol. 13, pp. 3945–3977, 2013, doi: [10.5194/acp-13-3945-2013](https://doi.org/10.5194/acp-13-3945-2013).
- [29] O. Ilic, P. Bermel, G. Chen, J. D. Joannopoulos, I. Celanovic, and M. Soljačić, "Tailoring high-temperature radiation and the resurrection of the incandescent source," *Nature Nanotechnol.*, vol. 11, pp. 320–324, 2016, doi: [10.1038/nnano.2015.309](https://doi.org/10.1038/nnano.2015.309).
- [30] X. Wang et al., "An improved electrophoretic deposition method for wafer level white PC-LED array packaging," *J. Display Technol.*, vol. 12, pp. 1609–1612, 2016, doi: [10.1109/JDT.2016.2614260](https://doi.org/10.1109/JDT.2016.2614260).